DiffRF: Rendering-Guided 3D Radiance Field Diffusion

Norman Müller[1,2]   Yawar Siddiqui[1,2]   Lorenzo Porzi[2]   Lorenzo Porzi[2]   Samuel Rota Bulò[2]

Peter Kontschieder[2]   Matthias Nießner[1]

Technical University of Munich[1]   Meta Reality Labs Zurich[2]
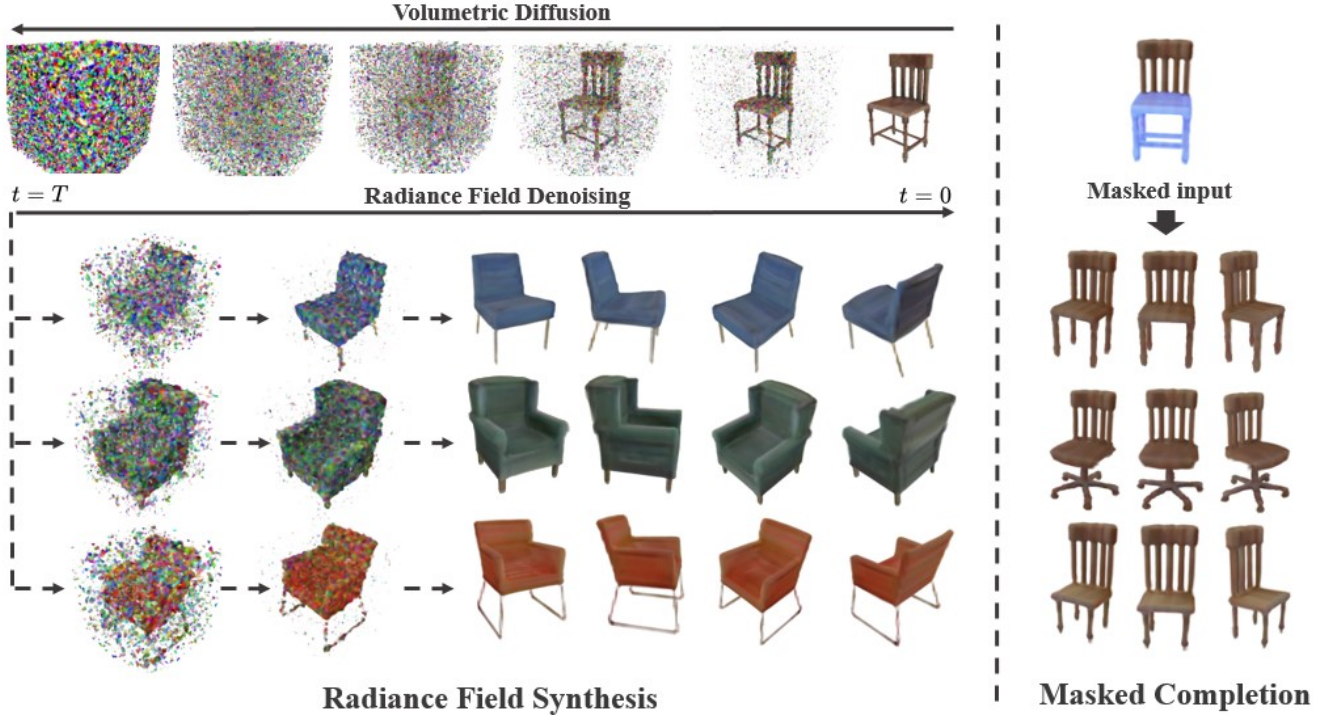
Figure 1. Our method performs denoising of a probabilistic diffusion process applied to 3D radiance fields. Guided by 3D supervision and volumetric rendering, our model enables the unconditional synthesis of high-fidelity 3D assets (left). We further introduce the novel application of masked completion (right), *i.e.*, the task of recovering shape and appearance from incomplete objects (highlighted in light-blue on the top right chair), solved by our model as conditional inference without task-specific training.

Abstract

We introduce DiffRF, a novel approach for 3D radiance field synthesis based on denoising diffusion probabilistic models. While existing diffusion-based methods operate on images, latent codes, or point cloud data, we are the first to directly generate volumetric radiance fields. To this end, we propose a 3D denoising model which directly operates on an explicit voxel grid representation. However, as radiance fields generated from a set of posed images can be ambiguous and contain artifacts, obtaining ground truth radiance field samples is non-trivial. We address this challenge by pairing the denoising formulation with a rendering loss, enabling our model to learn a deviated prior that favours good image quality instead of trying to replicate fitting er-

rors like floating artifacts. In contrast to 2D-diffusion models, our model learns multi-view consistent priors, enabling free-view synthesis and accurate shape generation. Compared to 3D GANs, our diffusion-based approach naturally enables conditional generation such as masked completion or single-view 3D synthesis at inference time.

1. Introduction

In recent years, Neural Radiance Fields (NeRFs) [39] have emerged as a powerful representation for fitting individual 3D scenes from posed 2D input images. The ability to photo-realistically synthesize novel views from arbitrary viewpoints while respecting the underlying 3D scene geom-

Project page: https://sirwyver.github.io/DiffRF/.

1

etry has the potential to disrupt and transform applications like AR/VR, gaming, mapping, navigation, *etc*. A number of recent works have introduced extensions for making NeRFs more sophisticated, by *e.g*., showing how to incorporate scene semantics [19, 31], training models from heterogeneous data sources [37], or scaling them up to represent large-scale scenes [65, 67]. These advances are testament to the versatility of ML-based scene representations; however, they still fit to specific, individual scenes rather than generalizing beyond their input training data.

In contrast, neural field representations that generalize to multiple object categories or learn priors for scenes across datasets appear much more limited to date, despite enabling applications like single-image 3D object generation [7, 41, 51, 69, 75] and unconstrained scene exploration [16]. These methods explore ways to disentangle object priors into shape and appearance-based components, or to decompose radiance fields into several small and locally-conditioned radiance fields to improve scene generation quality; however, their results still leave significant gaps w.r.t. photorealism and geometric accuracy.

Directions involving generative adversarial networks (GANs) that have been extended from the 2D domain to 3D-aware neural fields generation are demonstrating impressive synthesis results [8]. Like regular 2D GANs, the training objective is based on discriminating 2D images, which are obtained by rendering synthesized 3D radiance fields.

At the same time, diffusion-based models [54] have recently taken the computer vision research community by storm, performing on-par or even surpassing GANs on multiple 2D benchmarks, and are producing photo-realistic images that are almost indistinguishable from real photographs. For multi-modal or conditional settings such as text-to-image synthesis, we currently observe unprecedented output quality and diversity from diffusion-based approaches. While several works address purely geometric representations [35, 78], lifting the denoising-diffusion formulation directly to 3D volumetric radiance fields remains challenging. The main reason lies in the nature of diffusion models, which require a one-to-one mapping between the noise vector and the corresponding ground truth data samples. In the context of radiance fields, such volumetric ground truth data is practically infeasible to obtain, since even running a costly per-sample NeRF optimization results in incomplete and imperfect radiance field reconstructions.

In this work, we present the first diffusion-based generative model that directly synthesizes 3D radiance fields, thus unlocking high-quality 3D asset generation for both shape and appearance. Our goal is to learn such a generative model trained across objects, where each sample is given by a set of posed RGB images.

To this end, we propose a 3D denoising model directly operating on an explicit voxel grid representation (Fig. 1, left) producing high-frequency noise estimates. To address the ambiguous and imperfect radiance field representation for each training sample, we propose to bias the noise prediction formulation from Denoising Diffusion Probabilistic Models (DDPMs) towards synthesizing higher image quality by an additional volumetric rendering loss on the estimates. This enables our method to learn radiance field priors less prone to fitting artifacts or noise accumulation during the sampling process. We show that our formulation leads to diverse and geometrically-accurate radiance field synthesis producing efficient, realistic, and view-consistent renderings. Our learned diffusion prior can be applied in an unconditional setting where 3D object synthesis is obtained in a multi-view consistent way, generating highly-accurate 3D shapes and allowing for free-view synthesis. We further introduce the new task of *conditional masked completion* – analog to shape completion – for radiance field completion at inference time. In this setting, we allow for realistic 3D completion of partially-masked objects without the need for task-specific model adaptation or training (see Fig. 1, right). We summarize our contributions as follows:

- To the best of our knowledge, we introduce the first diffusion model to operate directly on 3D radiance fields, enabling high-quality, truthful 3D geometry and image synthesis.
- We introduce the novel application of 3D radiance field masked completion, which can be interpreted as a natural extension of image inpainting to the volumetric domain.
- We show compelling results in unconditional and conditional settings, *e.g*., by improving over GAN-based approaches on image quality (from 16.54 to 15.95 in FID) and geometry synthesis (improving MMD from 5.62 to 4.42), on the challenging PhotoShape Chairs dataset [46].

2. Related work

Diffusion models. Since the seminal work by Sohl-Dickstein *et al*. [54] on generative diffusion modeling, two classes of generative models have been proposed that perform inversion of a diffusion process: Denoising Score Matching (DSM) [55, 58, 59] and Denoising Diffusion Probablistic Models (DDPMs) [24]. Both approaches have shown to be flavours of a single framework, coined Score SDE, in the work of Song *et al*. [60]. The term "Diffusion models" is now being used as an all-encompassing name for this constellation of methods. Several main directions being studied include devising different sampling schemes [29, 56] and noising models [15, 26], exploring alternative formulations and training algorithms [27, 43, 57], and improving efficiency [50]. An overview of current research results is given by Karras *et al*. [29].

Diffusion models have been used to obtain state-of-the-art results in many domains such as text-to-image and guided synthesis [38, 42, 47, 50], 3D shape generation [6, 35, 77, 78], molecule prediction [36, 66, 72], and video generation [25, 74]. Interestingly, diffusion models have shown to outperform Generative Adversarial Networks (GANs) in high-resolution image generation tasks [17, 50], achieving unprecedented results in conditional image generation [49]. Furthermore, compared to GANs, which are often prone to divergence and mode collapse [5, 40], diffusion models have been observed to be much easier to train, although training time is still relatively long.

3D generation. Initially developed for 2D image synthesis, adversarial approaches have also found success in 3D, *e.g.*, for generating meshes [20, 71], 3D textures [53], voxelized representations [10, 22], or Neural Radiance Fields (NeRFs) [7, 8, 21, 44, 51, 79]. In particular, methods in this last category have received much attention in recent years, as they can be trained purely from collections of 2D images, without any form of 3D supervision, and enable for the first time photo-realistic novel view synthesis of the generated 3D objects. Pi-GAN [7] and GRAF [51] propose similar approaches where a standard NeRF [39] model is cast in a GAN setting by adding a form of stochastic conditioning, trained with an adversarial loss. These approaches are partly limited by the high training-time memory cost of NeRF-style volumetric rendering, forcing them to use low-resolution image patches. CIPS-3D [79] and GIRAFFE [44] solve this issue by letting the volume rendering component output a low-resolution 2D feature map, which is then upsampled by an efficient convolutional network to produce the final image. This approach drastically improves the quality and resolution of the rendered images, but also introduces 3D inconsistencies, as the convolutional stage can process different views of the same object in arbitrarily different ways. StyleNeRF [21] partially addresses this problem by carefully designing the convolutional stage to minimize inconsistencies, while EG3D [8] further improves on training efficiency by replacing the MLP-based NeRF with a light-weight tri-plane volumetric model generated by a convolutional network. In contrast to our method, these GAN-based approaches do not naturally support conditional synthesis or completion.

Compared to GANs, diffusion models are relatively under-explored as a tool for 3D synthesis, but a few works have emerged in the past two years. Some diffusion based-generators have been proposed for 3D point clouds [6, 35, 77, 78], showing promising results for conditional synthesis, completion, and other related tasks [77, 78]. DreamFusion [47], 3DDesigner [32], and GAUDI [3], like our work, employ diffusion models in conjunction with radiance fields, with applications in both conditional (on text and images) and unconditional 3D generation. DreamFu-

sion [47] presents an algorithm to generate NeRFs, augmented with an illumination component, by optimizing a loss defined by a pre-trained 2D text-conditional diffusion model. GAUDI [3] builds a 3D scene generator by first training a conditional NeRF to reconstruct a set of indoor videos given scene-specific latents, and then fitting a diffusion model to capture the learned latent space. Concurrent works like [2, 70] apply the denoising-diffusion approach to factorized radiance representations. In contrast, our diffusion model operates directly in the space of radiance fields which directly enables 3D-conditional tasks like shape completion (Sec. 4.2) by leveraging the learned volumetric prior.

3. Method

Our method consists of a generative model for 3D objects that builds on recent state-of-the-art diffusion probabilistic models [24]. It is trained to revert a process that gradually corrupts 3D objects by injecting noise at different scales. In our case, 3D objects are represented as radiance fields [39], so the learned denoising process allows our method to generate object radiance fields from noise.

Since we target the generation of 3D objects as radiance fields, we begin with a brief overview of this representation before delving into the details of our method.

3.1. Radiance Fields

A radiance field (σ, ξ) is an implicit, volumetric representation of a 3D object that is given in terms of a density field $\sigma : \mathcal{X} \to \mathbb{R}_+$ and an RGB color field $\xi : \mathcal{X} \to \mathbb{R}^3$ defined over a 3D domain $\mathcal{X} \subset \mathbb{R}^3$.[1] The density field gives information about the presence of an object in a specific point in space, whereas the color field provides the eventual corresponding RGB color.

Following a ray casting logic, the radiance field can be rendered along a given ray r yielding an RGB color c_r with the following equation [39]

$$c_r := \int_0^\infty \tau_s(r)\sigma(r_s)\xi(r_s)ds \,, \qquad (1)$$

where a ray r is a linear curve parametrized by s with unit velocity, $r_s \in \mathcal{X}$ denotes the point along the ray at s, and $\tau_s(r)$ is the transmittance probability at s, which is given by

$$\tau_s(r) := \exp\left(-\int_0^s \sigma(s')ds'\right) \,. \qquad (2)$$

Using the ray rendering equation above, we can render the radiance field from any given camera, yielding an image of the novel view. It is sufficient to turn the camera into a proper set of rays expressed in world coordinates.

---

[1]Typically the color field spans also the viewing direction, but we omit it in this work.
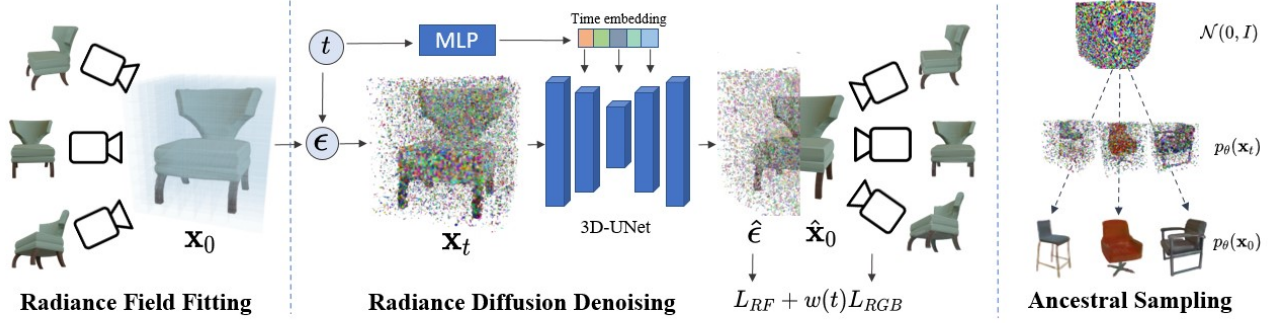
Figure 2. For a time step t uniformly sampled from $1, ..., T$, we first diffuse an initial radiance field f_0 according to a fixed noising schedule. The resulting f_t is passed through a time-conditioned 3D-UNet, giving an estimate of the applied noise ϵ. We guide the model by the noise prediction loss L_{RF} as well as a rendering loss L_{RGB} on the predicted denoising $\tilde{f}_0$.

There exist various ways of implementing a radiance field, ranging from neural networks [39] to explicit voxel grids [28,61]. In this work, we opt for the latter, since it enables good rendering quality along with faster training and inference. The explicit grid can be queried at continuous positions via bilinear interpolation of the voxel vertices.

Under the explicit representation, radiance fields become 4D tensors, where the first three dimensions index a grid spanning $\mathcal{X}$, whereas the last dimension indexes the density and color channels.

3.2. Generating Radiance Fields

Following recent advancements in the context of denosing-based generative methods [24], we formulate our generative model of radiance fields as a denoising diffusion probabilistic model.

Generation process. The generation (*a.k.a.* denoising) process is governed by a discrete-time Markov chain defined on the state space $\mathcal{F}$ of all possible pre-activated radiance fields expressed as flattened 4D tensors of fixed size.[2] The chain has a finite number of time steps $\{0, \ldots, T\}$. The denoising process starts by sampling a state f_T from a standard, multivariate normal distribution $p(f_T) \coloneqq \mathcal{N}(f_T|0, I)$, and generates states f_{t-1} from f_t by leveraging reversed transition probabilities $p_\theta(f_{t-1}|f_t)$ that are Gaussian with learned parameters θ. Specifically we have

$$p_\theta(f_{t-1}|f_t) \coloneqq \mathcal{N}(f_{t-1}|\mu_\theta(f_t, t), \Sigma_t). \tag{3}$$

The generation process iterates up to the final state f_0, which represents the radiance field of a 3D object generated by our method. The mean of the Gaussian in (3) can be directly modeled with a neural network. However, as we

will see later, it is more convenient to consider the following reparametrization of it

$$\mu_\theta(f_t, t) \coloneqq a_t(f_t - b_t \epsilon_\theta(f_t, t)), \tag{4}$$

where $\epsilon_\theta(f_t, t)$ is the noise that has been used to corrupt f_{t-1} predicted by *e.g.* a neural network, whereas a_t and b_t are pre-defined coefficients. Also the covariance Σ_t takes a pre-defined value, although it could be data-dependent. Additional details about the value that the pre-defined variables take are given in Sec. 3.3.

Diffusion process. While the generation process works by iteratively denoising a completely random radiance field, the diffusion process works the other way around and iteratively corrupts samples from the distribution of 3D objects we want to model. We introduce it because it plays a fundamental role in the training scheme of the generation process. The diffusion process is governed by a discrete-time Markov chain with the same state space and time bounds mentioned in the generation process but with Gaussian transition probabilities that are pre-defined and given by

$$q(f_t|f_{t-1}) \coloneqq \mathcal{N}(f_t|\sqrt{\alpha_t}f_{t-1}, \beta_t I), \tag{5}$$

where $\alpha_t \coloneqq 1 - \beta_t$ and $0 \leq \beta_t \leq 1$ are predefined coefficients implementing a schedule for the injected noise variance. The process starts by picking f_0 from the distribution $q(f_0)$ of 3D object radiance fields we want to model, iteratively samples f_t given f_{t-1} yielding a scaled and noise-corrupted version of the latter, and stops with f_T being typically close to completely random depending on the implemented noise-variance schedule. By exploiting properties of the Gaussian distribution, we can conveniently express the distribution of f_t conditioned on f_0 directly as a Gaussian distribution, yielding

$$q(f_t|f_0) = \mathcal{N}(f_t|\sqrt{\bar{\alpha}_t}f_0, (1 - \bar{\alpha}_t)I), \tag{6}$$

where $\bar{\alpha}_t \coloneqq \prod_{i=1}^{t} \alpha_i$. This relation will be useful to quickly generate diffused data points at arbitrary time steps.

---

[2]We consider pre-activated radiance fields, where both density and RGB color channels span a linear space and we assume a proper activation function will be applied at the time of rendering. This is required to have additive noise, while preserving a valid radiance field representation.

3.3. Training Objective

Our training objective comprises two complementary losses: i) A loss L_{RF} that penalizes the generation of radiance fields that do not fit the data distribution, and ii) an RGB loss L_{RGB} geared towards improving the quality of renderings from generated radiance fields.

Radiance field generation loss. Following [24], we derive the training objective for our model starting from a variational upper-bound on the Negative Log-Likelihood (NLL). This upper-bound requires specifying a surrogate distribution that we refer to as q because it indeed corresponds to the distribution q governing the diffusion process, establishing the anticipated fundamental link with the generation process. We provide here some key steps of the derivation of the bound and refer to [24] for more details about the intermediate ones. By Jensen inequality, the NLL of a data point $f_0 \in \mathcal{F}$ can be upper-bounded by leveraging q as follows:

$$-\log p_\theta(f_0) \leq \mathbb{E}_q\left[-\log \frac{p_\theta(f_{0:T})}{q(f_{1:T}|f_0)}\right] := L_{\text{RF}}(f_0|\theta),\tag{7}$$

where $f_{t_1:t_2}$ stands for $(f_{t_1}, \ldots, f_{t_2})$. The loss $L_{\text{RF}}(f_0|\theta)$ bounding the NLL can be further decomposed into the following sum, up to a constant independent from θ

$$L_{\text{RF}}(f_0|\theta) = \sum_{t=1}^{T} L_{\text{RF}}^t(f_0|\theta) + \text{const}.\tag{8}$$

Here, $L_{\text{RF}}^t(f_0|\theta)$ takes a simple and intuitive form if we set $a_t := \frac{1}{\sqrt{\alpha_t}}$ and $b_t := \frac{\beta_t}{\sqrt{1-\bar{\alpha}_t}}$ in (4), and pick $\Sigma_t := \frac{\beta_t^2}{2\alpha_t(1-\bar{\alpha}_t)}I$. Indeed, it yields

找出 ft 的 noise

$$L_{\text{RF}}^t(f_0|\theta) := \mathbb{E}_q\left[\|\epsilon - \epsilon_\theta(f_t, t)\|^2\right]$$

因為把 q distribution 的參數寫進式子裡，下標就可以改成表示 multivariate 的 normal distribution 的 phi

$$= \mathbb{E}_\phi\left[\|\epsilon - \epsilon_\theta(\sqrt{\bar{\alpha}_t}f_0 + \sqrt{1-\bar{\alpha}_t}\epsilon, t)\|^2\right],$$

where $\phi(\epsilon) := \mathcal{N}(\epsilon|0, I)$ is the probability distribution of ϵ, namely a normal multivariate, and the last equality follows from (6).

Radiance field rendering loss. We complement the previous loss with an additional RGB loss $L_{\text{RGB}}(f_0|\theta)$, aimed at improving the quality of renderings from generated radiance fields. Indeed, the Euclidean metric on the representation that is implicitly used in the previous loss to assess the quality of generated radiance fields does not necessarily ensure the absence of artifacts once we try to render the radiance field. We define $L_{\text{RGB}}(f_0|\theta)$ as a sum of time-specific terms $L_{\text{RGB}}^t(f_0|\theta)$ similar to (8), yielding

$$L_{\text{RGB}}(f_0|\theta) := \sum_{t=1}^{T} L_{\text{RGB}}^t(f_0|\theta).\tag{9}$$

Given a radiance field $f \in \mathcal{F}$, a viewpoint v, we denote by $R(v, f)$ the image obtained after rendering f from viewpoint v using equation (1). We also denote by $\ell_v(f, I)$ the Euclidean distance between the rendered images from viewpoint v using radiance fields f and the ground-truth image I_v from the view-point v, *i.e.*

$$\ell_v(f, I) := \|I_v - R(v, f)\|^2.\tag{10}$$

The idea is to compare the rendering of a given radiance field f_0 sampled from the data distribution corrupted with t diffusion steps and then fully denoised against the original ground-truth image I_v used to obtain f_0. In theory, this implies sampling first f_t from $q(f_t|f_0)$ and then sampling back f_0 from $p_\theta(f_0|f_t)$. This is, however, computationally demanding and we resort to a simpler approximation. From the definition of L_{RF}^t, the loss pushes towards having $\epsilon \approx \epsilon_\theta(f_t, t)$ from which we can derive the approximation $\tilde{f}_0^t(\epsilon, \theta) := f_0 + \frac{\sqrt{1-\bar{\alpha}_t}}{\sqrt{\bar{\alpha}_t}}(\epsilon - \epsilon_\theta(f_t, t))$. We can then define our rendering loss as

$$L_{\text{RGB}}^t(f_0|\theta) := \omega_t \mathbb{E}_{\phi,\psi}\left[\ell_v(\tilde{f}_0^t(\epsilon, \theta), I)\right],\tag{11}$$

where the expectation is taken with respect to a prior distribution ψ for the viewpoint v and $\epsilon \sim \phi(\epsilon)$. Since the approximation is reasonable only with steps t close to zero, we introduce a weight w_t that decays as step values increase (*e.g.* we use $\omega_t := \bar{\alpha}_t^2$). We provide evidence in the experimental section that despite being an approximation, the proposed loss contributes to significantly improving the results.

Final loss. To summarize, the final training loss per data point f_0 is given by the weighted combination of the radiance field generation and rendering losses introduced before, with a small variation that enables stochastic sampling of the step t from a uniform distribution $\kappa(t)$:

$$L(\theta) := L_{\text{RF}}(f_0|\theta) + \lambda_{\text{RGB}} L_{\text{RGB}}(f_0|\theta)$$
$$\propto \mathbb{E}_\kappa\left[L_{\text{RF}}^t(f_0|\theta) + \lambda_{\text{RGB}} L_{\text{RGB}}^t(f_0|\theta)\right].$$

Implementation details We implement ϵ_θ as a 3D-UNet, which is based on the 2D-UNet architecture introduced in [17] by replacing 2D convolutions and attention layers with corresponding 3D operators. For training, we uniformly sample timesteps $t = 1, \ldots, T = 1000$ for all experiments with variances of the diffusion process linearly increasing from $\beta_1 = 0.0015$ to $\beta_T = 0.05$, and choose to weight the rendering loss L_{RGB}^t with $w_t = \bar{\alpha}_t^2$. We refer to the supplementary material for additional details.

4. Experiments

In this section, we evaluate the performance of our method on both unconditional and conditional radiance field generation.

Datasets. We run experiments on the PhotoShape Chairs [46] and on the Amazon Berkeley Objects (ABO) Tables dataset [12]. For PhotoShape Chairs, we render the provided 15,576 chairs using Blender Cycles [13] from 200 views on an Archimedean spiral. For ABO Tables, we use the provided 91 renderings with 2-3 different environment map settings per object, resulting in 1676 tables. Since both datasets do not provide radiance field representations of 3D objects, we generate them using a voxel-based approach at a resolution of 32^3 from the multi-view renderings.

Metrics. We evaluate image quality using the Fréchet Inception Distance [23] (FID) and Kernel Inception Distance [4] (KID) using [45]. For comparison of the geometrical quality, we follow [1] and compute the Coverage Score (COV) and Minimum Matching Distance (MMD) using Chamfer Distance (CD). While the Coverage Score measures the diversity of the generated samples, MMD assesses the quality of the generated samples. All metrics are evaluated at a resolution of 128×128.

4.1. Unconditional Radiance Field Synthesis

Comparison against state of the art. We quantitatively evaluate our approach on the task of unconditional 3D synthesis on PhotoShape [46] in Tab. 1 and ABO Tables [12] in Tab. 2. We compare against leading methods for 3D-aware image synthesis: π-GAN [7] and EG3D [8]. Both our method and GAN-based approaches use the same set of rendered images for training. While we pre-process the rendered images to create a radiance field representation for each of the shape samples, the GAN-based methods are trained directly on the rendered images.

Compared to these approaches, our method yields overall better image quality while achieving significant improvements in geometrical quality and diversity. Fig. 3 and Fig. 4 show a qualitative comparison of our method with π-GAN and EG3D. While EG3D achieves good image quality, it tends to produce inaccurate shapes and view-dependent image artifacts, like adding or removing armrests or changing the supporting structure. As the training objective (see Sec. 3.3) is to invert the diffusion process to denoise towards detailed volumetric representations, we observe that DiffRF reliably generates radiance fields with fine photo-metric and geometrical details.

Contribution of the rendering loss. Tab. 1 and Tab. 2 show ablation results where we evaluate the effects of 2D supervision on the radiance synthesis. Removing 2D supervision ("DiffRF w/o 2D", line 3 in the tables), as expected, has a noticeable effect on FID, which increases by ≈ 2.3 for PhotoShape and by ≈ 8.8 for ABO Tables. This shows that biasing the noise prediction formulation from DDPM by a volumetric rendering loss leads to higher image quality. Qualitative comparisons can be found in the appendix. We

Method	FID ↓	KID ↓	COV ↑	MMD ↓
π-GAN [7]	52.71	13.64	39.92	7.387
EG3D [8]	16.54	8.412	47.55	5.619
DiffRF w/o 2D	18.27	9.263	**59.20**	4.543
DiffRF	**15.95**	**7.935**	58.93	**4.416**

Table 1. Quantitative comparison of unconditional generation on the PhotoShape Chairs [46] dataset. Our method achieves a better image and geometric quality than state-of-the-art GAN-based approaches. The additional 2D rendering loss improves image quality as indicated by the drop in quality without it. MMD and KID scores are multiplied by 10^3.

Method	FID ↓	KID ↓	COV ↑	MMD ↓
π-GAN [7]	41.67	13.81	44.23	10.92
EG3D [8]	31.18	11.67	48.15	9.327
DiffRF w/o 2D	35.89	13.94	**63.46**	8.013
DiffRF	**27.06**	**10.03**	61.54	**7.610**

Table 2. Quantitative comparison of unconditional generation on the ABO Tables [12] dataset. Our method achieves a better image and geometric quality than state-of-the-art GAN-based approaches, with the 2D rendering loss being important. MMD and KID scores are multiplied by 10^3.

	Masking:	20%	40%	60%	80%	Avg
mPSNR↑	EG3D	23.71	24.86	24.92	25.79	24.82
	DiffRF	24.85	26.66	28.23	30.38	**27.53**
FID→	EG3D	25.91	29.41	33.06	34.31	30.67
	DiffRF	22.36	27.74	31.16	29.84	**27.78**

Table 3. Quantitative evaluation on the task of radiance field completion at different levels of masking. EG3D struggles to faithfully reconstruct non-masked regions of the original sample, while our method maintains the non-masked regions and synthesises coherent completions for the masked regions.

notice a decrease in the Coverage Score that we explain by the fact that the rendering loss guides the denoising model towards learning radiance fields with less artifacts, thus reducing the amount of diverse but spurious shapes.

4.2. Conditional Generation

GANs need to be trained in order to be conditioned on a particular task, while diffusion models can be effectively conditioned at test-time [17, 34, 60]. We leverage this property for the novel task of masked radiance field completion.

Masked Radiance Field Completion. Shape completion and image inpainting are well-studied tasks [63, 73, 76, 78] aiming to fill missing regions within a geometrical representation or in an image, respectively. We propose to combine
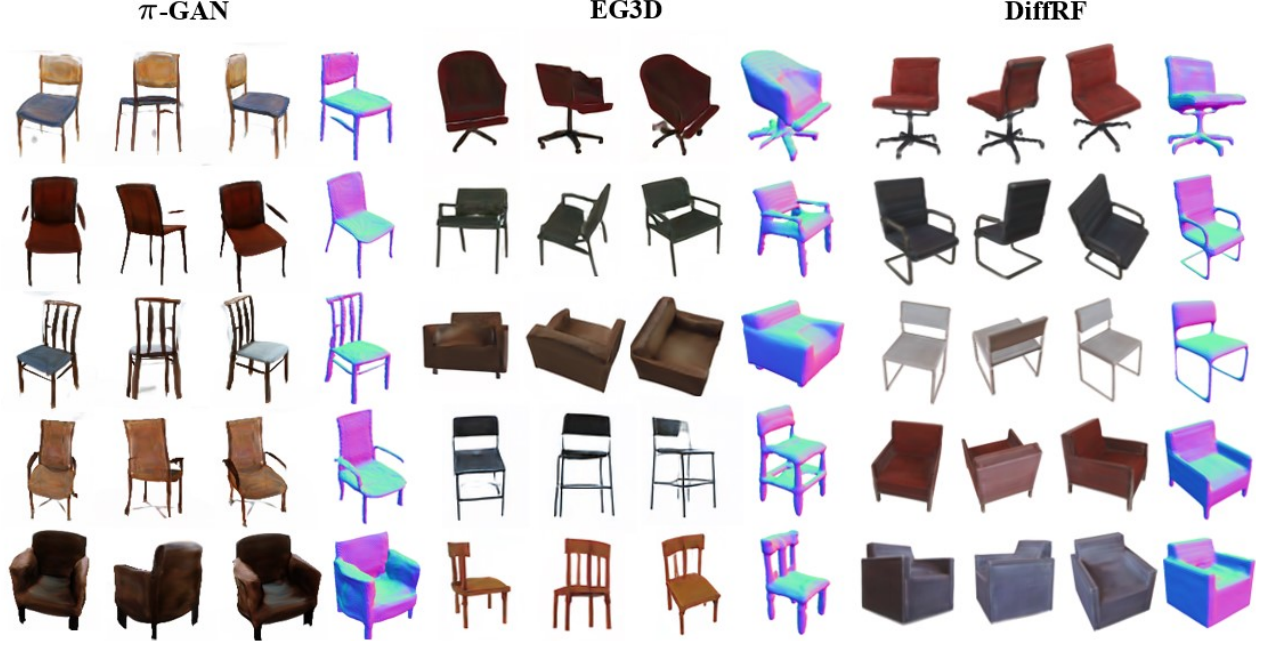
Figure 3. Qualitative comparison between π-GAN [7], EG3D [8], and our method on PhotoShape Chairs [46]. Our approach leads to diverse, geometrically accurate models that allow for high-quality renderings.
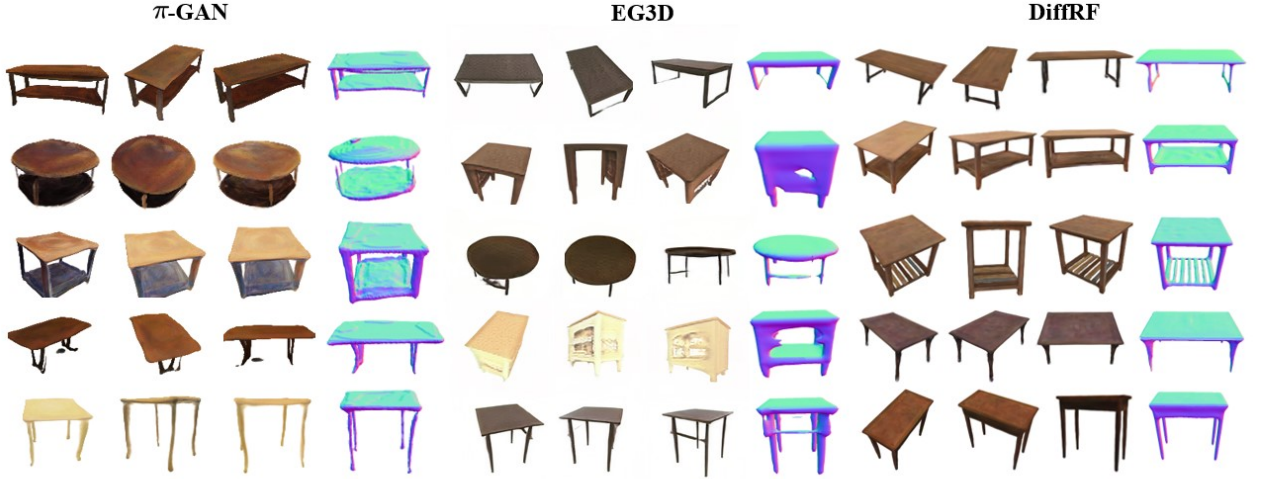

Figure 4. Qualitative comparison between π-GAN [7], EG3D [8], and our method on ABO Tables [12]. Our approach generates high quality and diverse samples with accurate geometry.

both in the novel task of masked radiance field completion: Given a radiance field and a 3D mask, synthesize a completion of the masked region that harmonizes with the non-masked region. Inspired by RePaint [34], we perform conditional completion by gradually guiding the unconditional sampling process in the known region to the input f^{in}

$$f_0^{t-1} = \sqrt{\bar{\alpha}_t}(m \odot \tilde{f}_0^t + (1-m) \odot f^{in})$$
$$f_{t-1} \sim \mathcal{N}(f_0^{t-1}, (1-\bar{\alpha}_t)I),$$

where m is a binary mask applied to the input (light blue

in Fig. 6) and $\odot$ denotes element-wise multiplication on the voxel grid.

A quantitative analysis of the masking performance is shown in Tab. 3, where we compare our method against EG3D at different levels of masking. At each level, we randomly mask 200 samples and evaluate the completion performance in terms of FID (by rendering from 10 random views), as well as the photo-metric accuracy of unmasked regions (mPSNR). For EG3D, we use masked GAN inversion, where we perform global latent optimization (GLO)
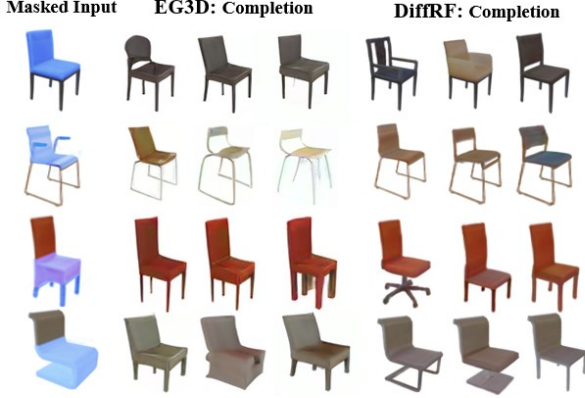
7

Figure 5. Qualitative completion of masked chairs from Photo-Shape [46]. DiffRF shows more diverse proposals compared to EG3D, while also maintaining the original non-masked regions.
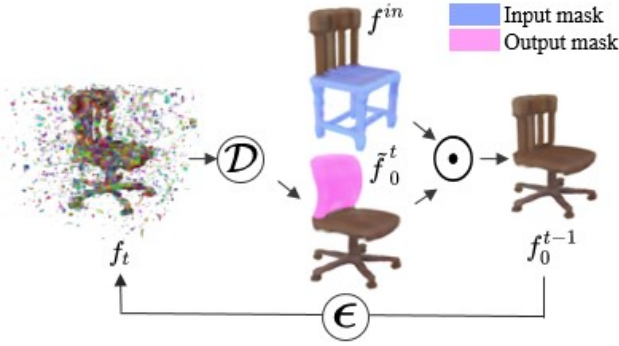

Figure 6. Masked radiance field completion. For a trained denoiser $\mathcal{D}$ and a given a radiance field with a 3D masked region (shown in blue), completion can be obtained by iteratively fusing the non-masked input region with the estimated denoisings $\tilde{f}_0^t$ and applying the diffusion process on the resulting f_0^{t-1}.

to minimize the photo-metric error on the re-projected, unmasked regions. We notice that, due to the single latent code representation, EG3D struggles to faithfully reconstruct the unmasked region of the input sample, and regularization is needed to not corrupt the overall representation. Fig. 5 further shows a qualitative comparison of the masking performance against EG3D.

Image-to-Volume Synthesis. DiffRF can be used to obtain 3D radiance fields from single view images by steering the sampling process using volumetric rendering. For this, we adopt the Classifer Guidance formulation from [17] to guide the denoising process towards minimizing the rendering error against a posed RGB image with corresponding object mask (obtained, for example, with off-the-shelf segmentation networks). Fig. 7 shows qualitative results for this single-image reconstruction task on chairs from Scan-Net [14]. Furthermore, we show results of our model conditioned on CLIP-embeddings [48] in the appendix.
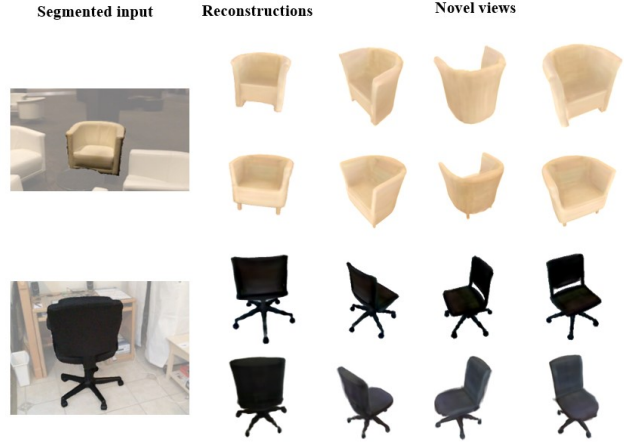
這裡的 guidance 就是在 denoise 的過程裡，也加入 RGB image 的資訊，幫助生成出跟 single image 相關的 RF

Figure 7. Qualitative synthesis results of single-view reconstruction on ScanNet [14]. Given a single posed image and its foreground mask, our method can recover meaningful proposals for the radiance fields describing the objects (shown in separate rows).

4.3. Limitations

While our method shows promising results on the tasks of conditional and unconditional radiance field synthesis, several limitations remain. Compared to GAN-based approaches, our radiance fields-based approach requires a sufficient number of posed views in order to generate good training samples and suffers from lower sampling times. In this context, it would be interesting to explore leveraging faster sampling methods [30]. Finally, our model is constrained in the maximum grid resolution by training-time memory limitations. These could be addressed by exploring adaptive [64, 68] or sparse grid structures [18, 52, 64] as well as factorized neural fields representations [9, 70].

5. Conclusions

We introduce DiffRF – a novel approach for 3D radiance field synthesis based on denoising diffusion probabilistic models. To the best of our knowledge, DiffRF is the first generative diffusion-based method to operate directly on volumetric radiance fields. Our model learns multi-view consistent priors from collections of posed images, enabling free-view image synthesis and accurate shape generation. We evaluated DiffRF on several object classes, comparing its performance against state-of-the-art GAN-based approaches, and demonstrating its effectiveness in both conditional and unconditional 3D generation tasks.

Acknowledgements

References

[1] Panos Achlioptas, Olga Diamanti, Ioannis Mitliagkas, and Leonidas Guibas. Learning representations and generative models for 3d point clouds. In *International conference on machine learning*, pages 40–49. PMLR, 2018. 6

[2] Titas Anciukevicius, Zexiang Xu, Matthew Fisher, Paul Henderson, Hakan Bilen, Niloy J. Mitra, and Paul Guerrero. RenderDiffusion: Image diffusion for 3D reconstruction, inpainting and generation. *arXiv*, 2022. 3

[3] Miguel Angel Bautista, Pengsheng Guo, Samira Abnar, Walter Talbott, Alexander Toshev, Zhuoyuan Chen, Laurent Dinh, Shuangfei Zhai, Hanlin Goh, Daniel Ulbricht, et al. Gaudi: A neural architect for immersive 3d scene generation. *arXiv preprint arXiv:2207.13751*, 2022. 3

[4] Mikołaj Bińkowski, Dougal J. Sutherland, Michael Arbel, and Arthur Gretton. Demystifying MMD GANs. In *International Conference on Learning Representations*, 2018. 6

[5] Andrew Brock, Jeff Donahue, and Karen Simonyan. Large scale gan training for high fidelity natural image synthesis. *arXiv preprint arXiv:1809.11096*, 2018. 3

[6] Ruojin Cai, Guandao Yang, Hadar Averbuch-Elor, Zekun Hao, Serge J. Belongie, Noah Snavely, and Bharath Hariharan. Learning gradient fields for shape generation. *CoRR*, abs/2008.06520, 2020. 3

[7] Eric Chan, Marco Monteiro, Petr Kellnhofer, Jiajun Wu, and Gordon Wetzstein. pi-gan: Periodic implicit generative adversarial networks for 3d-aware image synthesis. In *arXiv*, 2020. 2, 3, 6, 7

[8] Eric R. Chan, Connor Z. Lin, Matthew A. Chan, Koki Nagano, Boxiao Pan, Shalini De Mello, Orazio Gallo, Leonidas Guibas, Jonathan Tremblay, Sameh Khamis, Tero Karras, and Gordon Wetzstein. Efficient geometry-aware 3D generative adversarial networks. In *CVPR*, 2022. 2, 3, 6, 7, 12

[9] Anpei Chen, Zexiang Xu, Andreas Geiger, Jingyi Yu, and Hao Su. Tensorf: Tensorial radiance fields. *arXiv preprint arXiv:2203.09517*, 2022. 8

[10] Kevin Chen, Christopher B Choy, Manolis Savva, Angel X Chang, Thomas Funkhouser, and Silvio Savarese. Text2shape: Generating shapes from natural language by learning joint embeddings. In *Asian conference on computer vision*, pages 100–116. Springer, 2018. 3

[11] Yen-Chi Cheng, Hsin-Ying Lee, Sergey Tuyakov, Alex Schwing, and Liangyan Gui. SDFusion: Multimodal 3d shape completion, reconstruction, and generation. *arXiv*, 2022. 14

[12] Jasmine Collins, Shubham Goel, Kenan Deng, Achleshwar Luthra, Leon Xu, Erhan Gundogdu, Xi Zhang, Tomas F Yago Vicente, Thomas Dideriksen, Himanshu Arora, et al. Abo: Dataset and benchmarks for real-world 3d object understanding. In *Proceedings of the IEEE/CVF Conference on Computer Vision and Pattern Recognition*, pages 21126–21136, 2022. 6, 7, 12, 14, 16

[13] Blender Online Community. *Blender - a 3D modelling and rendering package*. Blender Foundation, Stichting Blender Foundation, Amsterdam, 2018. 6

[14] Angela Dai, Angel X Chang, Manolis Savva, Maciej Halber, Thomas Funkhouser, and Matthias Nießner. Scannet: Richly-annotated 3d reconstructions of indoor scenes. In *Proceedings of the IEEE conference on computer vision and pattern recognition*, pages 5828–5839, 2017. 8

[15] Giannis Daras, Mauricio Delbracio, Hossein Talebi, Alexandros G Dimakis, and Peyman Milanfar. Soft diffusion: Score matching for general corruptions. *arXiv preprint arXiv:2209.05442*, 2022. 2

[16] Terrance DeVries, Miguel Angel Bautista, Nitish Srivastava, Graham W. Taylor, and Joshua M. Susskind. Unconstrained scene generation with locally conditioned radiance fields. In *Proceedings of the IEEE/CVF Conference on Computer Vision and Pattern Recognition (ICCV)*, 2021. 2

[17] Prafulla Dhariwal and Alexander Nichol. Diffusion models beat gans on image synthesis. *Advances in Neural Information Processing Systems*, 34:8780–8794, 2021. 3, 5, 6, 8, 12, 13, 14

[18] Sara Fridovich-Keil, Alex Yu, Matthew Tancik, Qinhong Chen, Benjamin Recht, and Angjoo Kanazawa. Plenoxels: Radiance fields without neural networks. In *Proceedings of the IEEE/CVF Conference on Computer Vision and Pattern Recognition*, pages 5501–5510, 2022. 8

[19] Xiao Fu, Shangzhan Zhang, Tianrun Chen, Yichong Lu, Lanyun Zhu, Xiaowei Zhou, Andreas Geiger, and Yiyi Liao. Panoptic nerf: 3d-to-2d label transfer for panoptic urban scene segmentation. In *International Conference on 3D Vision (3DV)*, 2022. 2

[20] Jun Gao, Tianchang Shen, Zian Wang, Wenzheng Chen, Kangxue Yin, Daiqing Li, Or Litany, Zan Gojcic, and Sanja Fidler. Get3d: A generative model of high quality 3d textured shapes learned from images. *arXiv preprint arXiv:2209.11163*, 2022. 3

[21] Jiatao Gu, Lingjie Liu, Peng Wang, and Christian Theobalt. Stylenerf: A style-based 3d-aware generator for high-resolution image synthesis. *arXiv preprint arXiv:2110.08985*, 2021. 3

[22] Philipp Henzler, Niloy J Mitra, and Tobias Ritschel. Escaping plato's cave: 3d shape from adversarial rendering. In *Proceedings of the IEEE/CVF International Conference on Computer Vision*, pages 9984–9993, 2019. 3

[23] Martin Heusel, Hubert Ramsauer, Thomas Unterthiner, Bernhard Nessler, and Sepp Hochreiter. Gans trained by a two time-scale update rule converge to a local nash equilibrium. *Advances in neural information processing systems*, 30, 2017. 6

[24] Jonathan Ho, Ajay Jain, and Pieter Abbeel. Denoising diffusion probabilistic models. *arXiv preprint arxiv:2006.11239*, 2020. 2, 3, 4, 5

[25] Jonathan Ho, Tim Salimans, Alexey Gritsenko, William Chan, Mohammad Norouzi, and David J Fleet. Video diffusion models. *arXiv preprint arXiv:2204.03458*, 2022. 3

[26] Emiel Hoogeboom and Tim Salimans. Blurring diffusion models. *arXiv preprint arXiv:2209.05557*, 2022. 2

[27] Chin-Wei Huang, Jae Hyun Lim, and Aaron C Courville. A variational perspective on diffusion-based generative models and score matching. *Advances in Neural Information Processing Systems*, 34:22863–22876, 2021. 2

[28] Animesh Karnewar, Tobias Ritschel, Oliver Wang, and Niloy Mitra. Relu fields: The little non-linearity that could. In *ACM SIGGRAPH 2022 Conference Proceedings*, SIGGRAPH '22, New York, NY, USA, 2022. Association for Computing Machinery. 4

[29] Tero Karras, Miika Aittala, Timo Aila, and Samuli Laine. Elucidating the design space of diffusion-based generative models. In *Proc. NeurIPS*, 2022. 2

[30] Zhifeng Kong and Wei Ping. On fast sampling of diffusion probabilistic models. *arXiv preprint arXiv:2106.00132*, 2021. 8

[31] Abhijit Kundu, Kyle Genova, Xiaoqi Yin, Alireza Fathi, Caroline Pantofaru, Leonidas J Guibas, Andrea Tagliasacchi, Frank Dellaert, and Thomas Funkhouser. Panoptic neural fields: A semantic object-aware neural scene representation. In *Proceedings of the IEEE/CVF Conference on Computer Vision and Pattern Recognition*, 2022. 2

[32] Gang Li, Heliang Zheng, Chaoyue Wang, Chang Li, Changwen Zheng, and Dacheng Tao. 3ddesigner: Towards photorealistic 3d object generation and editing with text-guided diffusion models. *arXiv preprint arXiv:2211.14108*, 2022. 3

[33] William E Lorensen and Harvey E Cline. Marching cubes: A high resolution 3d surface construction algorithm. *ACM siggraph computer graphics*, 21(4):163–169, 1987. 12

[34] Andreas Lugmayr, Martin Danelljan, Andres Romero, Fisher Yu, Radu Timofte, and Luc Van Gool. Repaint: Inpainting using denoising diffusion probabilistic models. In *Proceedings of the IEEE/CVF Conference on Computer Vision and Pattern Recognition (CVPR)*, pages 11461–11471, June 2022. 6, 7

[35] Shitong Luo and Wei Hu. Diffusion probabilistic models for 3d point cloud generation. In *Proceedings of the IEEE/CVF Conference on Computer Vision and Pattern Recognition*, pages 2837–2845, 2021. 2, 3

[36] Shitong Luo, Chence Shi, Minkai Xu, and Jian Tang. Predicting molecular conformation via dynamic graph score matching. *Advances in Neural Information Processing Systems*, 34:19784–19795, 2021. 3

[37] Ricardo Martin-Brualla, Noha Radwan, Mehdi S. M. Sajjadi, Jonathan T. Barron, Alexey Dosovitskiy, and Daniel Duckworth. NeRF in the Wild: Neural Radiance Fields for Unconstrained Photo Collections. In *Proceedings of the IEEE/CVF Conference on Computer Vision and Pattern Recognition (CVPR)*, 2021. 2

[38] Chenlin Meng, Yutong He, Yang Song, Jiaming Song, Jiajun Wu, Jun-Yan Zhu, and Stefano Ermon. SDEdit: Guided image synthesis and editing with stochastic differential equations. In *International Conference on Learning Representations*, 2022. 3

[39] Ben Mildenhall, Pratul P Srinivasan, Matthew Tancik, Jonathan T Barron, Ravi Ramamoorthi, and Ren Ng. Nerf: Representing scenes as neural radiance fields for view synthesis. In *European conference on computer vision*, pages 405–421. Springer, 2020. 1, 3, 4

[40] Takeru Miyato, Toshiki Kataoka, Masanori Koyama, and Yuichi Yoshida. Spectral normalization for generative adversarial networks. *arXiv preprint arXiv:1802.05957*, 2018. 3

[41] Norman Müller, Andrea Simonelli, Lorenzo Porzi, Samuel Rota Bulò, Matthias Nießner, and Peter Kontschieder. Autorf: Learning 3d object radiance fields from single view observations. In *Proceedings of the IEEE/CVF Conference on Computer Vision and Pattern Recognition (CVPR)*, 2022. 2

[42] Alex Nichol, Prafulla Dhariwal, Aditya Ramesh, Pranav Shyam, Pamela Mishkin, Bob McGrew, Ilya Sutskever, and Mark Chen. GLIDE: towards photorealistic image generation and editing with text-guided diffusion models. *CoRR*, abs/2112.10741, 2021. 3

[43] Alexander Quinn Nichol and Prafulla Dhariwal. Improved denoising diffusion probabilistic models. In *International Conference on Machine Learning*, pages 8162–8171. PMLR, 2021. 2

[44] Michael Niemeyer and Andreas Geiger. Giraffe: Representing scenes as compositional generative neural feature fields. In *Proceedings of the IEEE/CVF Conference on Computer Vision and Pattern Recognition*, pages 11453–11464, 2021. 3

[45] Anton Obukhov, Maximilian Seitzer, Po-Wei Wu, Semen Zhydenko, Jonathan Kyl, and Elvis Yu-Jing Lin. High-fidelity performance metrics for generative models in pytorch, 2020. Version: 0.3.0, DOI: 10.5281/zenodo.4957738. 6

[46] Keunhong Park, Konstantinos Rematas, Ali Farhadi, and Steven M. Seitz. Photoshape: Photorealistic materials for large-scale shape collections. *ACM Trans. Graph.*, 37(6), Nov. 2018. 2, 6, 7, 8, 12, 13, 15, 17, 19

[47] Ben Poole, Ajay Jain, Jonathan T Barron, and Ben Mildenhall. Dreamfusion: Text-to-3d using 2d diffusion. *arXiv preprint arXiv:2209.14988*, 2022. 3

[48] Alec Radford, Jong Wook Kim, Chris Hallacy, Aditya Ramesh, Gabriel Goh, Sandhini Agarwal, Girish Sastry, Amanda Askell, Pamela Mishkin, Jack Clark, et al. Learning transferable visual models from natural language supervision. In *International conference on machine learning*, pages 8748–8763. PMLR, 2021. 8, 14

[49] Aditya Ramesh, Prafulla Dhariwal, Alex Nichol, Casey Chu, and Mark Chen. Hierarchical text-conditional image generation with clip latents. *arXiv preprint arXiv:2204.06125*, 2022. 3

[50] Robin Rombach, Andreas Blattmann, Dominik Lorenz, Patrick Esser, and Björn Ommer. High-resolution image synthesis with latent diffusion models, 2021. 2, 3

[51] Katja Schwarz, Yiyi Liao, Michael Niemeyer, and Andreas Geiger. Graf: Generative radiance fields for 3d-aware image synthesis. In *Advances in Neural Information Processing Systems (NeurIPS)*, 2020. 2, 3

[52] Katja Schwarz, Axel Sauer, Michael Niemeyer, Yiyi Liao, and Andreas Geiger. Voxgraf: Fast 3d-aware image synthesis with sparse voxel grids. In *Advances in Neural Information Processing Systems*. 8

[53] Yawar Siddiqui, Justus Thies, Fangchang Ma, Qi Shan, Matthias Nießner, and Angela Dai. Texturify: Generating textures on 3d shape surfaces. *arXiv preprint arXiv:2204.02411*, 2022. 3

[54] Jascha Sohl-Dickstein, Eric Weiss, Niru Maheswaranathan, and Surya Ganguli. Deep unsupervised learning using nonequilibrium thermodynamics. In *International Conference on Machine Learning*, pages 2256–2265. PMLR, 2015. 2

[55] Jiaming Song, Chenlin Meng, and Stefano Ermon. Denoising diffusion implicit models. *arXiv preprint arXiv:2010.02502*, 2020. 2

[56] Jiaming Song, Chenlin Meng, and Stefano Ermon. Denoising diffusion implicit models. In *International Conference on Learning Representations*, 2021. 2

[57] Yang Song, Conor Durkan, Iain Murray, and Stefano Ermon. Maximum likelihood training of score-based diffusion models. *Advances in Neural Information Processing Systems*, 34:1415–1428, 2021. 2

[58] Yang Song and Stefano Ermon. Generative modeling by estimating gradients of the data distribution. *CoRR*, abs/1907.05600, 2019. 2

[59] Yang Song and Stefano Ermon. Improved techniques for training score-based generative models. *Advances in neural information processing systems*, 33:12438–12448, 2020. 2

[60] Yang Song, Jascha Sohl-Dickstein, Diederik P Kingma, Abhishek Kumar, Stefano Ermon, and Ben Poole. Score-based generative modeling through stochastic differential equations. *arXiv preprint arXiv:2011.13456*, 2020. 2, 6

[61] Cheng Sun, Min Sun, and Hwann-Tzong Chen. Direct voxel grid optimization: Super-fast convergence for radiance fields reconstruction. In *CVPR*, 2022. 4

[62] Xingyuan Sun, Jiajun Wu, Xiuming Zhang, Zhoutong Zhang, Chengkai Zhang, Tianfan Xue, Joshua B Tenenbaum, and William T Freeman. Pix3d: Dataset and methods for single-image 3d shape modeling. In *Proceedings of the IEEE conference on computer vision and pattern recognition*, pages 2974–2983, 2018. 14, 18

[63] Roman Suvorov, Elizaveta Logacheva, Anton Mashikhin, Anastasia Remizova, Arsenii Ashukha, Aleksei Silvestrov, Naejin Kong, Harshith Goka, Kiwoong Park, and Victor Lempitsky. Resolution-robust large mask inpainting with fourier convolutions. *arXiv preprint arXiv:2109.07161*, 2021. 6

[64] Towaki Takikawa, Joey Litalien, Kangxue Yin, Karsten Kreis, Charles Loop, Derek Nowrouzezahrai, Alec Jacobson, Morgan McGuire, and Sanja Fidler. Neural geometric level of detail: Real-time rendering with implicit 3D shapes. 2021. 8

[65] Matthew Tancik, Vincent Casser, Xinchen Yan, Sabeek Pradhan, Ben Mildenhall, Pratul Srinivasan, Jonathan T. Barron, and Henrik Kretzschmar. Block-NeRF: Scalable large scene neural view synthesis. In *Proceedings of the IEEE/CVF Conference on Computer Vision and Pattern Recognition (CVPR)*, 2022. 2

[66] Brian L Trippe, Jason Yim, Doug Tischer, Tamara Broderick, David Baker, Regina Barzilay, and Tommi Jaakkola. Diffusion probabilistic modeling of protein backbones in 3d for the motif-scaffolding problem. *arXiv preprint arXiv:2206.04119*, 2022. 3

[67] Haithem Turki, Deva Ramanan, and Mahadev Satyanarayanan. Mega-nerf: Scalable construction of large-scale nerfs for virtual fly-throughs. In *Proceedings of the IEEE/CVF Conference on Computer Vision and Pattern Recognition (CVPR)*, 2022. 2

[68] Peng-Shuai Wang, Yang Liu, Yu-Xiao Guo, Chun-Yu Sun, and Xin Tong. O-CNN: Octree-based Convolutional Neural Networks for 3D Shape Analysis. *ACM Transactions on Graphics (SIGGRAPH)*, 36(4), 2017. 8

[69] Qianqian Wang, Zhicheng Wang, Kyle Genova, Pratul P. Srinivasan, Howard Zhou, Jonathan T. Barron, Ricardo Martin-Brualla, Noah Snavely, and Thomas Funkhouser. Ibrnet: Learning multi-view image-based rendering. In *Proceedings of the IEEE/CVF Conference on Computer Vision and Pattern Recognition (CVPR)*, 2021. 2

[70] Tengfei Wang, Bo Zhang, Ting Zhang, Shuyang Gu, Jianmin Bao, Tadas Baltrusaitis, Jingjing Shen, Dong Chen, Fang Wen, Qifeng Chen, et al. Rodin: A generative model for sculpting 3d digital avatars using diffusion. *arXiv preprint arXiv:2212.06135*, 2022. 3, 8, 14

[71] Jiajun Wu, Chengkai Zhang, Tianfan Xue, Bill Freeman, and Josh Tenenbaum. Learning a probabilistic latent space of object shapes via 3d generative-adversarial modeling. *Advances in neural information processing systems*, 29, 2016. 3

[72] Minkai Xu, Lantao Yu, Yang Song, Chence Shi, Stefano Ermon, and Jian Tang. Geodiff: A geometric diffusion model for molecular conformation generation. *arXiv preprint arXiv:2203.02923*, 2022. 3

[73] Guandao Yang, Xun Huang, Zekun Hao, Ming-Yu Liu, Serge Belongie, and Bharath Hariharan. Pointflow: 3d point cloud generation with continuous normalizing flows. In *Proceedings of the IEEE/CVF International Conference on Computer Vision*, pages 4541–4550, 2019. 6, 12

[74] Ruihan Yang, Prakhar Srivastava, and Stephan Mandt. Diffusion probabilistic modeling for video generation. *arXiv preprint arXiv:2203.09481*, 2022. 3

[75] Alex Yu, Vickie Ye, Matthew Tancik, and Angjoo Kanazawa. pixelnerf: Neural radiance fields from one or few images. In *Proceedings of the IEEE/CVF Conference on Computer Vision and Pattern Recognition*, pages 4578–4587, 2021. 2

[76] Jiahui Yu, Zhe Lin, Jimei Yang, Xiaohui Shen, Xin Lu, and Thomas S Huang. Generative image inpainting with contextual attention. *arXiv preprint arXiv:1801.07892*, 2018. 6

[77] Xiaohui Zeng, Arash Vahdat, Francis Williams, Zan Gojcic, Or Litany, Sanja Fidler, and Karsten Kreis. Lion: Latent point diffusion models for 3d shape generation. *arXiv preprint arXiv:2210.06978*, 2022. 3, 14

[78] Linqi Zhou, Yilun Du, and Jiajun Wu. 3d shape generation and completion through point-voxel diffusion. In *Proceedings of the IEEE/CVF International Conference on Computer Vision*, pages 5826–5835, 2021. 2, 3, 6

[79] Peng Zhou, Lingxi Xie, Bingbing Ni, and Qi Tian. Cips-3d: A 3d-aware generator of gans based on conditionally-independent pixel synthesis. *arXiv preprint arXiv:2110.09788*, 2021. 3

11

Appendix

In this supplementary document, we discuss additional details about our method, the data used for training and evaluation, and show further qualitative results. We also refer to our for a comprehensive overview with further qualitative results.

A. Additional qualitative results

We provide additional qualitative results on PhotoShape Chairs [46] in Fig. 8 as well as on ABO Tables [12] in Fig. 9. Furthermore, we provide a qualitative comparison of our method when removing the rendering loss in Fig. 10 and Fig. 11.

B. Implementation detail

Architecture We base our architecture on 2D U-Net structure from [17]: For this, we replace the 2D convolutions in the ResNet and attention blocks with corresponding 3D convolutions, preserving kernel sizes and strides. Furthermore, we use 3D average pooling layers instead of 2D in the downsampling steps. Our U-Net consists of 4 scaling blocks with two ResNet blocks per scale, where we linearly increase the initial feature channel dimension of 64 to 256. We use skip attention blocks at the scaling factors 2, 4, and 8 with 32 channels per head.

Training details We train all models with a batch size of 8 and use the Adam optimizer with an initial learning of 10^{-4}. We apply a linear beta scheduling from 0.0015 to 0.05 at 1000 timesteps. From 4 random training views at a resolution of 128×128, we sample 8192 random pixels for the rendering supervision (with 92 z-steps for volumetric rendering) and weight the rendering loss with $\omega_t = \bar{\alpha}_t^2$. We train for 3.0m iterations with a decaying LR scheduling for 10^{-4} to 10^{-6} at a voxel grid resolution of 32 on 2 GPUs on every data set.

Sampling time We perform DDPM sampling for 1000 iterations leading to a run time of 48.6s per sample on an NVIDIA RTX 2080 TI. Once synthesized, our explicit representation enables rendering at 128×128 resolution with over 380 FPS.

C. Data

Radiance Field Generation For PhotoShape Chairs, we render the provided 15,576 chairs using Blender Cycles from 200 views on an Archimedean spiral at a fixed radius of 2.5 units with pitch starting from $-20°$ to $60°$. For ABO Tables, we use the provided 91 renderings with 2-3 different environment map settings per object, resulting in 1676 tables. For PhotoShape Chairs, we hold out 10%

of the samples for testing based on shape ids selected randomly, whereas for ABO Tables, we use the official data split. We fit explicit voxel grids at a resolution of 32^3 using volumetric rendering with spherical harmonics of degree 2 for an initial fit. We then fine-tune our representations for spherical harmonics of degree 0, which we found to lead to sharper geometry compared to directly optimizing density and color features. We furthermore bound the feature space to $[-1, 1]$ which we found to stabilize the sampling process noticeably affecting the rendering quality.

Evaluation For image quality evaluation, we calculate FID and IS by sampling 10k views by rendering 1000 samples from 10 random views at a resolution of 128×128. We follow [73] and evaluate the geometric quality by computing the Coverage Score (COV) and Minimum Matching Distance (MMD) using Chamfer Distance (CD)

$$\mathrm{CD}(X,Y) = \sum_{x \in X} \min_{y \in Y} ||x - y||_2^2 + \sum_{y \in Y} \min_{x \in X} ||x - y||_2^2,$$

$$\mathrm{COV}(S_g, S_r) = \frac{|\{\arg\min_{Y \in S_r} CD(X,Y) | X \in S_g\}|}{|S_r|},$$

$$\mathrm{MMD}(S_g, S_r) = \frac{1}{|S_r|} \sum_{Y \in S_r} \min_{X \in S_g} CD(X,Y),$$

on a reference set S_r (the test samples) and a generated set S_g twice as large as the reference set. We extract meshes using marching cubes [33] and sample 2048 points on the faces. To account for potentially different scaling of the samples produced by the 3D-aware GAN models, we normalize all point clouds by centering in the origin and anisotropic scaling of the extent to $[-1, 1]$.

For evaluation of the masked radiance field completion, we additionally compute a masked peak signal-to-noise ratio (mPSNR): Given a binary mask m of the input radiance field f^{in}, we compute for each corresponding input image the non-masked area by depth-based projection into the image plane using depth estimated from the input radiance field. We then compute the mPSNR by averaging the PSNR on the non-masked pixels for all evaluation views (we choose 10 views randomly).

D. Conditional sampling

Masked completion Since the generator of EG3D [8] is trained via 2D discriminator guidance, we perform 3D masked completion via GAN inversion. For this, we start from a random initial latent code and repeat the following steps for 200 iterations on each masked sample: We render the current synthesized sample from 8 views and project the 3D input mask onto the synthesized views using the predicted depths. On the remaining non-masked regions, we compute the photometric error with the input images. We

Figure 8. Additional qualitative sampling results on PhotoShape Chairs [46].

use the Adam optimizer with a learning rate of 10^{-2} with a small L_2 regularization term on the code (weighted with 5×10^{-2}) in order to update the latent code.

Image-to-Volume Synthesis Given a posed and segmented image, we condition our trained radiance field diffusion model by steering the sampling processing similar to the Classifier Guidance formulation from [17]: During sampling time, for each time step t, we gradually update the predicted denoised field $\tilde{f}_0^t$ towards minimizing the photometric error obtained from comparing the rendering $\tilde{I}_t$ from a given pose with the foreground-masked target image I. For this, we compute the gradient $\nabla_{\tilde{f}_0^t}(\tilde{I}_t, I)$ on the current denoising estimate by volumetric rendering and steer the

Figure 9. Additional qualitative sampling results on ABO Tables [12].

sampling process by $\tilde{f}_0^t \leftarrow \tilde{f}_0^t - \lambda \nabla_{\tilde{f}_0^t}(\tilde{I}_t, I)$ with a small guidance weight λ.

E. CLIP conditioning

Following related work [11,70,77], we additionally augment our model to condition on embeddings derived from text or single-image encodings obtained from CLIP ViT-B/32 [48] using cross-attention layers. For training, we use random single training views encoded by the frozen CLIP model to condition the denoiser. Here, we adapt the cross-attention mechanism from [17] for the 3D U-Net and do not train the image encoder in order to preserve the image-text-correspondence of CLIP. We show examples on single-image PhotoShape samples in Fig. 14 as well as on real-world image from the Pix3D dataset [62] in Fig. 13.

As these codes have strong correspondences to text samples by design, we can guide the sampling process by text prompts, examples are shown in Fig. 12 without the need for training on text-radiance field pairs.

DiffRF w/o 2D   **DiffRF**

Figure 10. Qualitative comparison on PhotoShape Chairs [46] when removing the 2D rendering loss.

DiffRF w/o 2D　　　　　**DiffRF**

Figure 11. Qualitative comparison on ABO Tables [12] when removing the 2D rendering loss.

a rustic simple wooden chair **a stool** **a green comfortable chair**

a leather chair **a purple chair** **chair with wheels**

Figure 12. Text-conditional inference using CLIP-embeddings trained on PhotoShape Chairs [46].

Figure 13. Image-conditional inference using CLIP-embeddings on Pix3D [62] images.

Figure 14. Image-conditional inference using single-view CLIP-embeddings on PhotoShape Chairs [46].